Available online at www.sciencedirect.com
SCIENCE DIRECT
Journal of Molecular Catalysis A: Chemical 249 (2006) 4–12
JOURNAL OF MOLECULAR CATALYSIS A: CHEMICAL
www.elsevier.com/locate/molcata

Aperiodic core structures of Pd and Pt giant clusters chemically stabilized with diphenyl phosphide ligands

Vladimir P. Oleshko *

Department of Materials Science & Engineering, University of Virginia, Charlottesville, VA 22904, USA

Received 17 October 2005; received in revised form 21 December 2005; accepted 21 December 2005
Available online 2 February 2006

Abstract

Atomic scale structures and compositions of "giant" clusters $[Pd_2(PPh_2)H_x]_n$, (**I**) and $[Pt(PPh_2)]_n$ (**II**) (PPh_2 = diphenyl phosphide, $n \cong 6$–10) and $Pd{\sim}_{561}Phen{\sim}_{60}(OAc){\sim}_{180}$ (**III**) (Phen = 1,10-phenanthroline; OAc = CH_3COO^-) have been investigated by high-resolution electron microscopy, electron diffraction and integrated field-emission analytical electron microscopy combining high-angle annular dark-field scanning transmission electron imaging, electron energy-loss spectroscopy (EELS) and windowless energy-dispersive X-ray nanoanalyses of metal cores and ligand shells. Observations revealed a uniform cell structure of the cluster matter with the unimodal core size distributions. Compositional deviations from the ideal stoichiometry were determined by EELS line profile analyses starting at the interfaces between cluster (**I**) cores and ligand shells. For clusters (**I**) and (**II**), with core sizes centered around 1.6 ± 0.3 nm and 1.5 ± 0.3 nm, respectively, lattice fringes and Debye–Scherrer diffraction rings were not observed, thus indicating that the structure within particles is not periodic. This was in contrast with the sputtered reference 1–2 nm Pt particles, which show clear evidence of crystallinity. Polyhedral Pd cores of clusters (**III**) with the diameter of 2.4 ± 0.3 nm also revealed lattice fringes assigned to an expanded face-centered cubic (fcc) structure, sometimes with multiple twinning. The structural differences suggest a ligand induced metal-to-molecular (non-crystalline) state transformation in clusters (**I**) and (**II**).

Keywords: Giant clusters; HRTEM; Integrated AEM

1. Introduction

The noble metal (M = Au, Pd, Rh, and Pt) polynuclear coordination compounds of Chini's type serve as a remarkable bridge between molecular clusters and metal colloids [1–4]. Their appearance has been predicted based on a "magic" number, $N = 1/3(10m^3 + 15m^2 + 11m + 3)$, of metal atoms filling a layer around the central atom or cluster core, where m is the number of metal layers in the packing of some possible symmetry types (cubooctahedral, anticubooctahedral, or icosahedral) [5]. The series of Chini's "magic" numbers, $N = 13$, 55, 147, 309, 561, ... correspond to $m = 1$, 2, 3, 4, 5, ..., respectively. The sizes of the metal cores of the cluster compounds are close to lower sizes of colloidal metal particles. However, chemically stabilized nanoclusters have a distinct ligand environment with a definite stoichiometry inherent to molecular clusters.

Interest in structures of the cluster compounds has increased in recent years in view of their unique catalytic selectivity under mild conditions towards a number of important redox reactions (photoelimination of hydrogen from water, hydrogenation of monocyclic arenes, oxidation, redox disproportionation and chain termination of alkenes, CO and alcohols [6–11], which open a way to the development of a new branch of catalysis by nanoclusters). Remarkable quantum-size effects in the thermodynamic properties of giant clusters [12,13] and attractive applications as electronic nanodevices (quantum dots [14,15]), nanofabricated planned cluster patterns [16], one- and two-dimensional (1D and 2D) self-assembled arrays of nanoclusters [17–19] and nanoporous alumina membranes [20] have been also reported. A key feature in structural characterization of such species (they are amorphous solids usually unsuitable for X-ray diffraction analysis) is to understand the relations between the atomic arrangement, electronic structure and chemical reactivity. In this regard, the effects of metal–ligand bonding and organic ligand-to-metal ratios on the cluster core structure that still remain essentially unclear, should be clarified.

* Tel.: +1 434 982 5659; fax: +1 434 982 5660.
E-mail address: vpo6n@virginia.edu.

1381-1169/$ – see front matter © 2006 Elsevier B.V. All rights reserved.
doi:10.1016/j.molcata.2005.12.029

Over last two decades high-resolution transmission electron microscopy (HRTEM) and scanning TEM (STEM) combined with nanometer resolution electron diffraction, energy-filtering TEM (EFTEM), electron energy-loss spectroscopy (EELS) and energy-dispersive X-ray (EDX) spectroscopy (so called analytical electron microscopy, AEM) have become major techniques for direct structural and analytical investigation of ultrafine particles [21]. By demonstrating the existence of polyhedral (dodecahedral and icosahedral) structures in multiple twinned nanoparticles of noble metals, HRTEM has provided probably the first instance that revealed the crucial role of surface forces in determining the overall particle structure. In addition, high spatial resolution EFTEM/EELS enables successful studies of transitions between outer-shell valence bands to the empty states above the Fermi level and related collective plasmon excitations in small particles between 0 eV and 25 eV energy loss. Another category of useful information can be obtained complementary to EDXS by recording of the core ionization edges above 25 eV, which relate unambiguously to the presence of given atom species. Furthermore, the detailed profile of the EEL spectrum on the ionization core threshold, energy-loss near-edge structure (ELNES) and extended energy-loss fine structure (EXELFS), is very sensitive to the oxidation state, local density of unoccupied states, bonding, coordination and crystal symmetry.

As a logical extension of a concept referred to as an integrated modular EM system, field-emission (FE)-AEM instruments combine in a design several electron imaging, diffraction and spectroscopic modes to provide analytical synergism having unique advantages over any single instrument down to sub-angstrom levels of lateral resolution, sub-electron volt energy resolution and single-atom analytical sensitivity [22,23]. This has made possible integrated digital data acquisition using flexible object oriented graphical user interfaces and various combinations of multiple detectors under the control of a powerful host processor. High-resolution *integrated FE-AEM* enables rapid and flexible acquisition of bright-field and high-angle annular dark field (HAADF) STEM and (EF) TEM images and diffraction patterns, series of EDX/EEL spectra and "live" on-line data evaluation and processing, e.g. with extraction of elemental profiles and maps (spectrum-imaging). However, to our knowledge there were no publications until present time describing applications of integrated FE-AEM particularly to giant clusters of noble metals and related cluster systems.

Earlier reported attempts on atomic-resolution TEM imaging particularly of $Au_{55}(PPh_3)_{12}Cl_6$ clusters were not successful because of their sensitivity to electron irradiation. Only lattice fringes from perfect Au nanocrystals formed during electron-beam induced decomposition of the clusters were observed [24]. Indeed, radiation damage of clusters followed a loss of organic ligands, rearrangement and agglomeration of metal cores that could occur during electron microscope observations, may significantly hamper HRTEM and AEM investigation [2]. Unlike palladium and gold, data on platinum "giant" clusters are still scarce and contradictory [25]. In this paper, we present atomic scale HRTEM observations of $[Pd_2(PPh_2)H_x]_n$, (**I**) and $[Pt(PPh_2)]_n$ (**II**) clusters (PPh_2 = diphenyl phos-

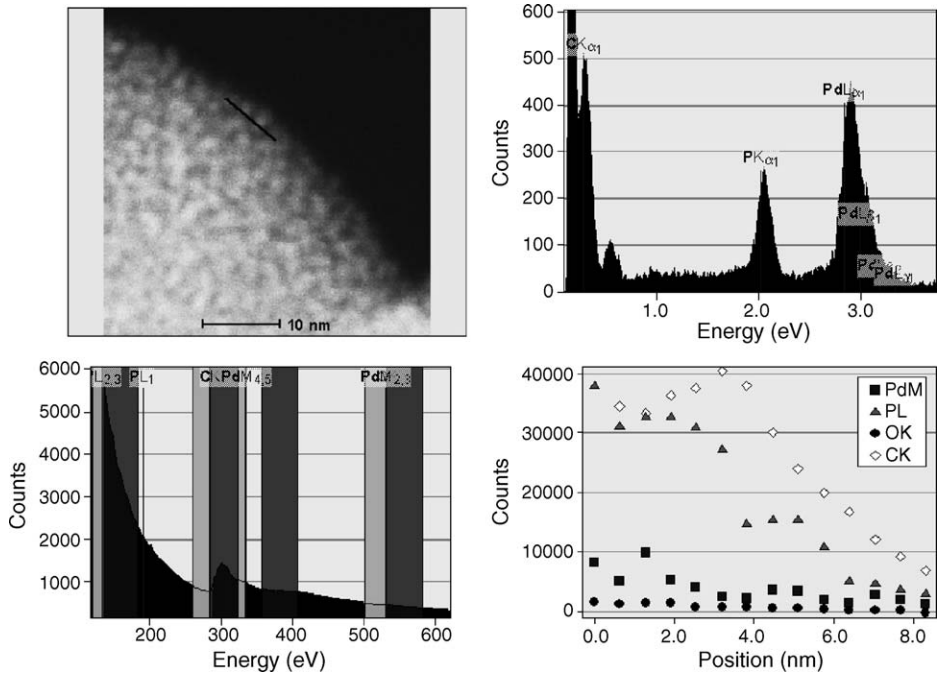

Fig. 1. Multiple-window user interface of an EmiSpec ES Vision acquisition system coupled a VG HB-501 dedicated field-emission STEM, a LINK AN-10000 EDXS analyzer and a GATAN 667 EEL spectrometer. The system enables one-click acquisition with pre-selected controls (brightness, contrast, gamma, dwell time, etc.) and processing of images, spectra, maps and line profiles: (upper left) HAADF-STEM image of clusters (**I**); (upper right) spot X-ray spectrum of a cluster (**I**) acquired in the same area, background subtracted, spectral lines fitted using three windows and the first order polynomial fitting; (bottom left) EEL spectrum of the clusters (**I**) acquired along the profile indicated by black line in the STEM image; (bottom right) Pd $M_{4,5}$-, P $L_{2,3}$-, C K- and O K-edge spectral intensities extracted from 14 EEL spectra along the line profile in the image. KLM-markers denote the lines of the elements of interest.

phide, $n \cong 6$–10, metal:ligand = 2:1 and 1:1, respectively) and $Pd{\sim}_{561}Phen{\sim}_{60}(OAc){\sim}_{180}$ (**III**) clusters (Phen = 1,10-phenanthroline; OAc = CH_3COO^-, metal:ligand ≈ 9.4) complemented by high-spatial resolution integrated compositional HAADF-FE-STEM/EELS/EDXS nanoanalyses that indicate a ligand induced metal-to-molecular (non-crystalline state) transformation in the metal cores of chemically stabilized Pd and Pt nanoclusters (**I**) and (**II**).

2. Experimental

Clusters (**I**) and (**II**) have been synthesized by reduction of corresponding arylphosphide–acetate M^{II} complexes [26]:

$$n[PPh_3Pd(OAc)_2]_2 \xrightarrow{n(x+5)HCOOH/C_6H_6} \underset{(\mathbf{I})}{[Pd_2PPh_2H_x]_n} + 4nHOAc + nPPh_3 + nC_6H_6 + n(x+5)CO_2 \quad (1)$$

$$n[PPh_3Pt(OAc)_2]_2 \xrightarrow{(3n+1)HCOOH/Ar} \underset{(\mathbf{II})}{2[(Ph_2P)Pt]_n} + 4nHOAc + 2nC_6H_6 + (3n+1)CO_2 \quad (2)$$

Here $n \cong 6$–10.

The giant Pd clusters (**III**) were prepared by the reduction of $Pd(OAc)_2$ with H_2 in acetic acid in the presence 1,10-phenanthroline, followed by treatment with O_2 [1,2]:

$$4nPd_3(OAc)_6 \xrightarrow{15nH_2,\,3nPhen/AcOH} 3[Pd_4Phen(OAc)_2H_4]_n + 18nHOAc, \quad n \approx 100 \quad (3)$$

$$[Pd_4Phen(OAc)_2H_4]_n \xrightarrow{O_2/AcOH} \underset{(\mathbf{III})}{Pd_{570\pm30}Phen_{60\pm3}(OAc)_{180}} \quad (4)$$

The material was mildly crushed and deposited onto carbon lacey and SiO_2 films supported by copper grids. HRTEM and SAED experiments were carried out on a JEOL-4000EX microscope at 400 kV accelerating voltage and point-to-point resolution of 0.17 nm. Windowless EDXS and EELS analyses and HAADF STEM imaging were performed using a VG HB-501 dedicated field-emission STEM at 100 kV accelerating voltage with a resolution of 0.4 nm equipped with a LINK AN-10000 EDXS analyzer and a GATAN 667 EEL spectrometer and coupled with an integrated EmiSpec ES Vision acquisition system (Fig. 1). Minimum beam intensities were used in order to prevent radiation damage of the specimens.

In order to extract net X-ray peak intensities, the spectrum background was subtracted and X-ray characteristic lines were fitted using three background windows followed by a first order polynomial fitting. EDX spectra have been quantified using a Cliff–Lorimer thin film ratio method with calculated *k*-factors,

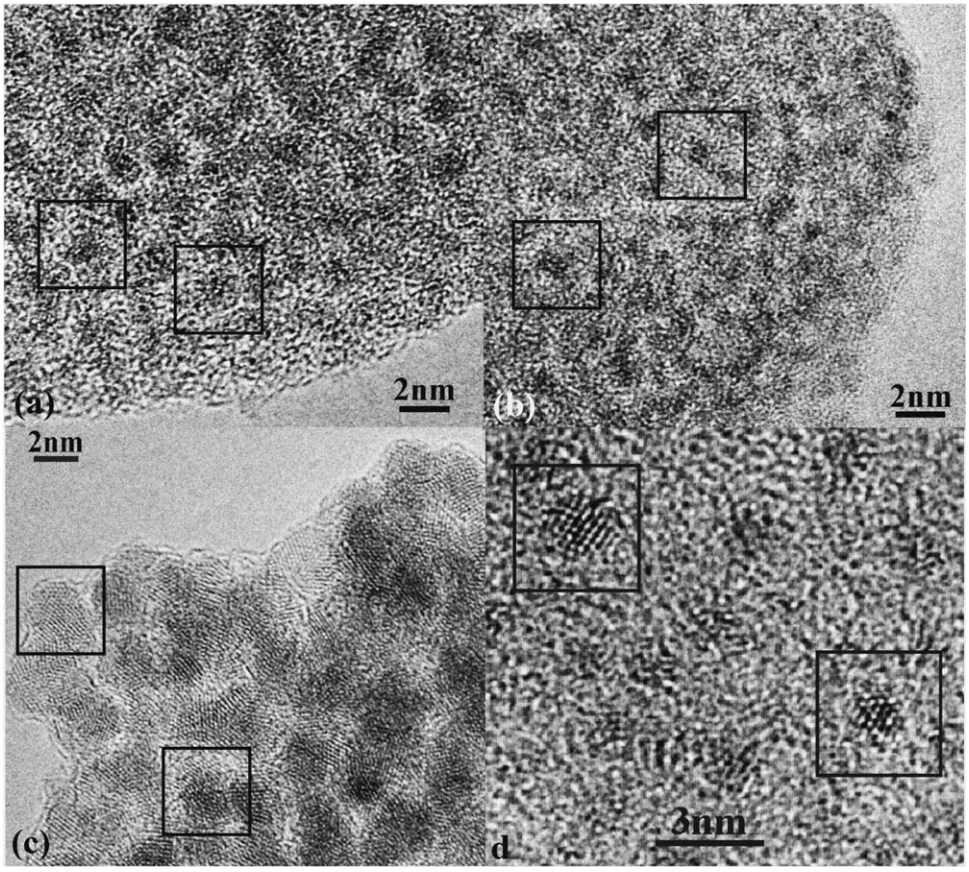

Fig. 2. HRTEM images of Pd and Pt giant clusters (**I**)–(**III**) and reference naked Pt nanoparticles: (a) (**I**); (b) (**II**); (c) (**III**); (d) thermally sputtered Pt particles of 1–2 nm in diameter. Black boxes mark individual non-crystalline (a and b) and crystalline Pd (c) and Pt (d) nanoparticles.

$k_{C(P)Pd}$ and absorption (thickness) correction, ACF [27–29]:

$$\frac{C_{Pd}}{C_{C(P)}} = \frac{k_{C(P)Pd}\,\mathrm{ACF} I_{Pd}}{I_{C(P)}} \quad (5)$$

Here C_{Pd} and $C_{C(P)}$ are the mass concentrations, and I are the net intensities of the characteristic X-ray α-lines for Pd, C and P, respectively; $k_{C(P)Pd} = [(Q\omega a)_{C(P)}/(Q\omega a)_{Pd}][A_{Pd}\varepsilon_{C(P)}/A_{C(P)}\varepsilon_{Pd}]$, where Q is the ionization cross-section, ω the fluorescence yield, a is the relative transition probability for the characteristic X-ray α-lines, A the atomic number and ε is the detector efficiency of the elements of interest:

$$\mathrm{ACF} = \left(\frac{\mu/\rho]^{C(P)}}{\mu/\rho]^{Pd}}\right)\left(\frac{1-\mathrm{e}^{-(\mu/\rho]^{Pd}\rho t\,\cos\mathrm{ec}\,\alpha)}}{1-\mathrm{e}^{-(\mu/\rho]^{C(P)}\rho t\,\cos\mathrm{ec}\,\alpha)}}\right),$$

where $\mu/\rho]^{Pd,C(P)}$ is the mass absorption coefficient for α-lines of the elements of interest, ρ the density of specimen, α the detector take-off angle and t is the specimen thickness.

For quantification of EEL spectra, the spectrum background was initially assigned assuming its power-law decay with a two window pre-edge fitting. Then, the spectral intensities were extracted with a 50 eV window from a series of EEL spectra along the line profile in a HAADF-STEM image shown by black

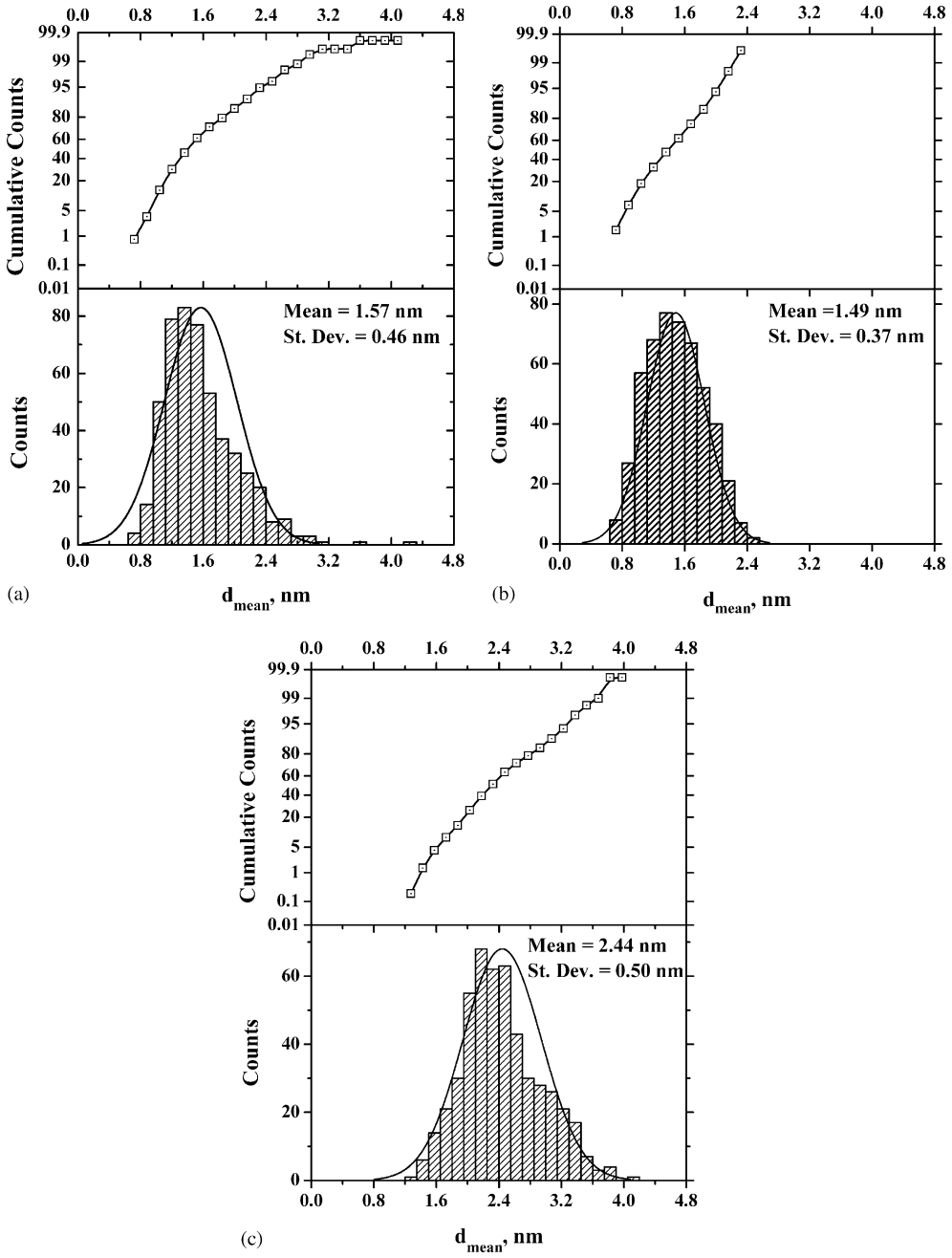

Fig. 3. Differential (bottom) and cumulative (top) histograms on size distributions on giant clusters (**I**)–(**III**), d_{mean} (nm) is the mean diameter of a metal core, 500 measurements. Continuous lines indicate normal curves with the given distribution parameters: (a) (**I**); (b) (**II**); (c) (**III**).

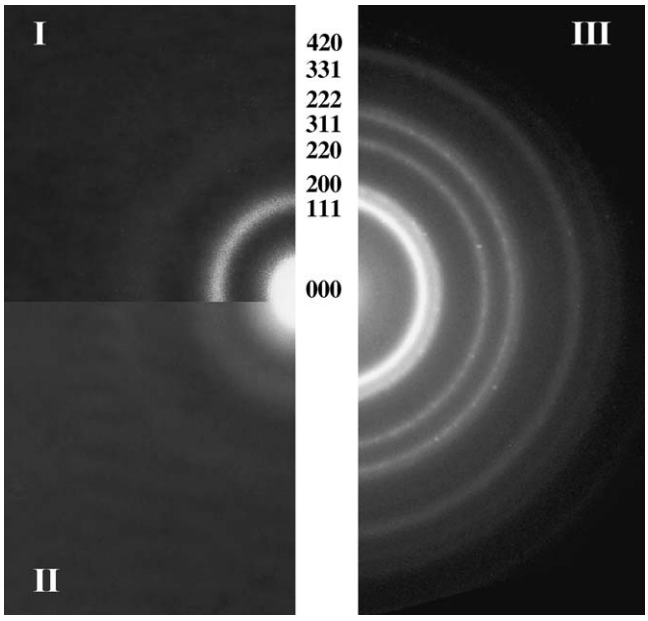

Fig. 4. SAED patterns of the giant clusters (**I**)–(**III**) with assigned reflecting planes for the fcc structure: upper left (**I**); bottom left (**II**); right (**III**).

lines in Fig. 1. The chemical compositions (in at.%) were converted from the net spectral intensities into atomic ratios by the ratio method followed normalization according to the equation [30]:

$$\frac{N_{\mathrm{Pd}}}{N_{\mathrm{C(P)}}} = \left[\frac{I_{\mathrm{PdM4,5}}(\beta, \Delta)}{I_{\mathrm{CK(PL2,3)}}(\beta, \Delta)}\right]\left[\frac{\sigma_{\mathrm{CK(PL2,3)}}(\beta, \Delta)}{\sigma_{\mathrm{(PdM4,5)}}(\beta, \Delta)}\right] \quad (6)$$

Here, $N_{\mathrm{Pd[C(P)]}}$ is the element areal density, $I_{\mathrm{PdM4,5,[CK(PL2,3)]}}$ the edge intensity, $\sigma_{\mathrm{PdM4,5[CK(PL2,3)]}}(\beta, \Delta)$ the integral cross-section of corresponding atoms, β the collection angle and Δ is the integration window. Estimates of the relevant cross-section were obtained from Gatan ELP software, version 3.0. For chosen working conditions ($E_0 = 100$ keV, $\beta = 39$ mrad, the convergent angle, $\alpha = 6.9$ mrad and $\Delta = 50$ eV), the following values for integral cross-sections for the C K-edge, the P $L_{2,3}$-edge and the $Pd_{M4,5}$-edges were calculated: σ_{CK} (39 mrad, 50 eV) = 6751 ± 675.1 barns, $\sigma_{\mathrm{PL2,3}}$ (39 mrad, 50 eV) = 55790 ± 557.9 barns and $\sigma_{\mathrm{PdM4,5)}}$ (39 mrad, 50 eV) = 6288 ± 628.8 barns, respectively.

3. Results

HRTEM micrographs in Fig. 2a–c exhibit metal cores of the clusters (**I**) and (**II**) forming a close packed cluster mat-

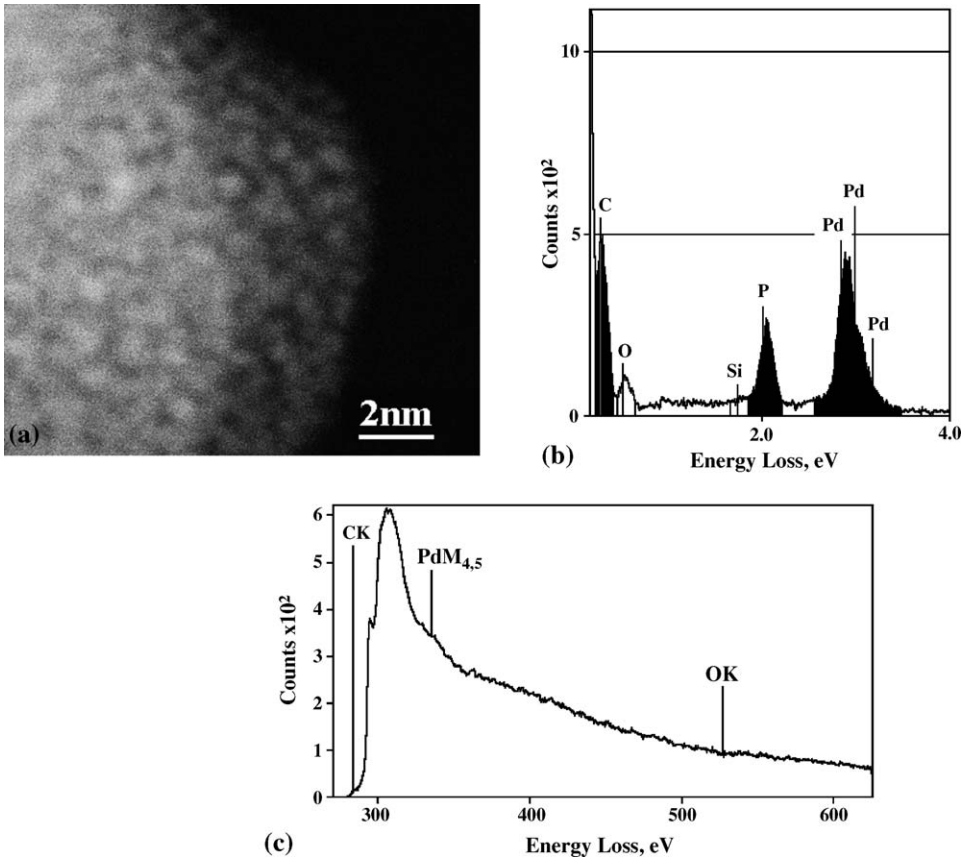

Fig. 5. (a) HAADF-STEM image of giant clusters (**I**), two neighboring areas exhibit slightly different contrast due to partial overlapping and varying mass-thickness; (b) their X-ray spectrum, lines of interest are marked; (c) EEL spectrum of the clusters (**I**) acquired in the same area along the line profile marked by white line in the image (a). The stripped CK-edge superimposed with the $PdM_{4,5}$-edge and the weak OK-edge from SiO_2 support is shown.

ter with an average diameter of 1.6 ± 0.3 nm and 1.5 ± 0.3 nm, respectively. In both cases, preferentially unimodal core size distributions can be fairly fitted with the normal curve (Fig. 3a and b). To avoid changes in the cluster samples due to ligand losses, rearrangement and/or agglomeration of metal cores, minimal beam intensities and short acquisition times were utilized. The clusters, unlike 1–2 nm diameter thermally sputtered reference Pt particles (Fig. 2d), showed no evidence of lattice fringes from spherical Pd and Pt cores. Their SAED patterns (Fig. 4) revealed only broad diffuse rings corresponding to the most probable interatomic distances between 0.23 nm and 0.25 nm (**I**) and between 0.23 nm and 0.28 nm (**II**) and weak rings at ~0.14 nm (**I** and **II**), respectively.

High-resolution HAADF-STEM imaging of the clusters (**I**) indicated that heavy metal atoms are concentrated within 1.2–1.8 nm diameter sphere-like clusters surrounded by ligand shells with no evidence of lattice fringes (Fig. 5a). On the contrary, the polyhedral Pd cores of clusters (**III**) of 2.4 ± 0.3 nm in diameter exhibit clearly lattice fringes with spacings consistent with the metal (1 1 1) planes as well as a series of diffraction

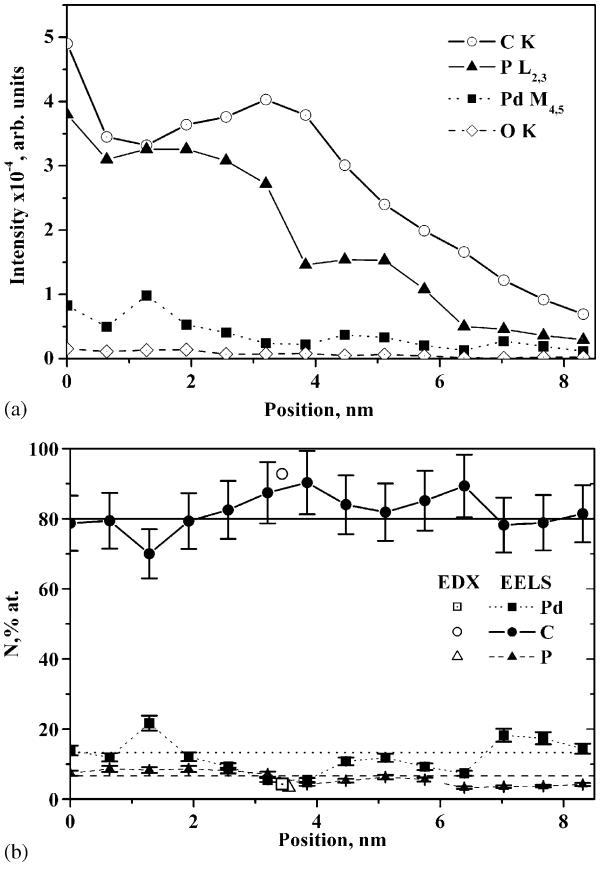

Fig. 6. (a) Pd $M_{4,5}$-, P $L_{2,3}$-, C K and O K-edge spectral intensities extracted from 14 EEL spectra of giant clusters (**I**). The spectra were acquired along a line profile in the image shown in Fig. 1. (b) The local chemical compositions of clusters (**I**) along the line profile converted from the net EEL intensities into atomic ratios by the ratio method followed normalization (solid points, bars denote an accuracy of ±10 at.%) and derived from the EDX spectrum in Fig. 5b by the Cliff–Lorimer thin ratio method (empty points at arbitrary chosen position). Horizontal lines show the ideal expected stoichiometry corresponding 13.3 at.% Pd, 6.67 at.% P and 80 at.% C, respectively.

Debye–Scherrer rings assigned to an expanded face-centered cubic (fcc) structure, sometimes with multiple twinning.

An X-ray spectrum of the clusters (**I**) in Fig. 5b revealed the Pd L-series (the Pd $L\alpha_1$ line at 2.84 keV, the Pd $L\beta_1$ line at 2.99 keV and the Pd $L\beta_2$ line at 3.17 keV) referred to the metal core and the C Kα line at 0.28 keV and the P K-series (the P $K\alpha_1$ at 2.02 keV, the P $K\alpha_2$ at 2.01 keV and the P $K\beta_1$ at 2.14 keV) assigned to the ligand shell. The O Kα line at 0.52 keV and the weak Si $K\alpha_1$ line at 1.74 keV generated from SiO_2 support and traces of copper (the Cu $L\alpha_1$ line at 0.93 keV) from a microscope grid were also found. The elemental composition of the clusters (**I**) estimated from the net intensities using the Cliff–Lorimer ratio method was 92.0 at.% C, 4.0 at.% P and 4.0 at.% Pd, respectively.

A PEEL spectrum of the clusters (**I**) acquired along the profile shown in Fig. 1 (Fig. 5c) presents the stripped C K-edge at 284 eV containing contributions both from π (285.5 eV) and σ (above 290 eV) C–C-bonding in PPh_2 ligands superimposed with the Pd $M_{4,5}$-edge at ~336 eV and the weak O K-edge at 532 eV from SiO_2 support. The spectrum background was assigned assuming its power-law decay with a two window pre-edge fitting. Fig. 6a shows the net Pd $M_{4,5}$-, P $L_{2,3}$-, C K- and O K-edge spectral intensities extracted with a 50 eV window from 14 EEL spectra along the line profile in Fig. 6a. Fig. 6b shows the chemical composition (in at.%) along the line profile converted from the net spectral intensities into atomic ratios by the ratio method followed normalization [30].

4. Discussion

HRTEM and HAADF-STEM imaging (Figs. 2a–c and 5a) demonstrate a quite uniform cell structure of the cluster matter (**I**) and (**II**) with core sizes centered around 1.6 ± 0.3 nm and 1.5 ± 0.3 nm, respectively. For HAADF-STEM, the differential cross-section of Rutherford elastic scattering is proportional to the square of the atomic number, Z^2 [28,29], thus giving a *Z*-contrast image that represents the cluster core structure in a rather straightforward way as bright spheres of 1.2–1.8 nm in diameter. Ligand shells are practically invisible here due to the much lower mean atomic number. Because of minimal beam intensities and short acquisition times under chosen experimental conditions, no visible changes in the cluster samples due to ligand losses, rearrangement and/or agglomeration of metal cores were found during observations. For both clusters (**I**) and (**II**) corresponding to relatively low metal-to-ligand rations (2:1 and 1:1, respectively), lattice fringes were not observed by HRTEM and HAADF-STEM. The direct observations show that the structure within spherical Pd and Pt cores is not periodic and it is essentially aperiodic. SAED patterns reveal only broad diffuse rings corresponding to the most probable interatomic distances between 0.23 nm and 0.25 nm (**I**) and between 0.23 nm and 0.28 nm (**II**) and weak rings at ~0.14 nm (**I** and **II**), respectively. According to EXAFS data [26], the distances of 0.21–0.22 nm are M–P (M = Pd, Pt) distances and ones of 0.25 nm (**I**) and of 0.28 nm (**II**) can be assigned to M–M distances. Due to inherent limitations of the technique, EXAFS

data, however, are averaged over the entire sample and usually require corrections for phase shift and amplitude and complicated fitting simulations [31].

On the contrary, phase contrast HRTEM and SAED, as spatially resolved techniques, enable to evaluate directly both statistical distributions of interatomic spacings and shapes and local crystallographic ordering/disordering of the cluster cores. This is illustrated by comparison of Fig. 2a–d. Unlike the clusters (**I**) and (**II**), thermally sputtered reference Pt nanoparticles of the same size range 1–2 nm show two-dimensional 0.23 nm {1 1 1} lattice fringes in a HRTEM image (Fig. 2d), thus unambiguously indicating crystallinity of individual Pt particles. For Pd giant clusters (**III**) stabilized with 1,10-phenanthroline ligands at the higher metal-to-ligand ratio of 9.4:1, mixed polyhedral (octahedral, cubooctahedral and icosahedral with characteristic pentad symmetry axis) shape Pd cluster cores also reveal multiple {1 1 1}-lattice fringes (Fig. 2c). Randomly oriented crystalline cores of the clusters (**III**) could exhibit some variations in apparent fringe spacing from 0.22 nm to 0.25 nm likely due to some expansion of the lattice and to edge effects and particle tilt as well [32]. A series of diffraction Debye–Scherrer rings in SAED patterns were assigned to an expanded face-centered cubic structure (Fig. 4). Discrete reflections corresponding to the cores larger than 7 nm in size were found occasionally. The unimodal core size distribution of the clusters (**III**) with the estimated average diameter of 2.4 ± 0.3 nm demonstrate a satisfactory fit with the normal curve (Fig. 3c). The observed core sizes match satisfactory to the expected magic number, $N = 1/3(10 \times 5^3 + 15 \times 5^2 + 11 \times 5 + 3) = 561$, of Pd atoms in the five-layer core [5]. The cluster matter displays local non-uniformity due to different packing of the metal cores and multiple twinning (not only icosahedral shapes, as it was initially suggested based on EXAFS analyses [1]) rather than variations in the core sizes. So, Figs. 2 and 4 suggest the distinct structural differences between thermally sputtered naked Pt nanoparticles and the clusters (**III**) on one hand and the clusters (**I**) and (**II**) on the other hand. This difference cannot be explained only by decreasing the average cluster sizes below 2.4 nm that might lead to a broadening of the diffraction rings. Diffuse scattering distributed over the expected positions of the Bragg reflections in the SAED patterns was likely caused by a non-periodic perturbation of the metal lattice in clusters (**I**) and (**II**) induced by surface reconstruction/relaxation due to the interaction with strong PPh_2 ligands [21].

Sub-nanometer electron probes generated using a FEG-STEM and integrated with digital spectral data acquisition allowed us to acquire 10–14 spectra and images under the control of the EmiSpec ES Vision digital acquisition system from any detector–spectrometer combination within a relatively short time (1–2 min). The chemical composition both of metal cores and PPh_2 ligand shells has been identified with sub-nanometer lateral resolution simultaneously by windowless EDXS and EELS spot and line profile nanoanalyses in the HAADF-STEM mode as illustrated in Fig. 5a–c. The net Pd $M_{4,5}$-, P $L_{2,3}$-, C K and O K-edge spectral intensities extracted from 14 EEL spectra of clusters (**I**) acquired along the line profile in Fig. 5a indicate local compositional variations when the probe crossing individual clusters and partially overlapping neighboring cluster dimers (maxima at positions of 1.5 nm, 5 nm and 7 nm, respectively, Fig. 6a). In general, estimations of the chemical composition of the clusters (**I**) along the line profile converted from the net EEL spectral intensities into atomic ratios with an accuracy of 10% (solid points, Fig. 6b) appeared to be in a fair agreement with the ideal stoichiometry (horizontal lines, Fig. 6b) and quantification of EDXS data (empty points at arbitrary chosen position, Fig. 5b). In the latter case, approximations made for the calculated *k*-factors (±20% relative [28]) and possible mass losses of organic ligands during analyses should be taken in account. On the other hand, compositional variations along the line profile at positions of 1.5 nm and 7 nm exceed ±10% limits (Fig. 6a and b), thus indicating local deviations from the ideal stoichiometry likely starting at the interfaces between Pd cores and ligand shells.

HRTEM and HAADF-STEM observations combined with local EELS/EDXS chemical analyses indicate that clusters (**I**) and (**II**) may have no exact chemical composition neither precise ordered structure, but rather composed of statistically distributed units with more or less narrow size and structure distributions similar to colloidal metals. However, the metal formal oxidation state in such species described by idealized models (see also reactions (1) and (2) in Section 2) can be non-integer as for the majority of individual metal clusters. Unusual aperiodic non-metallic structures of the clusters (**I**) and (**II**) may arise due to a transformation to a molecular (non-crystalline) state induced by the strong binding PPh_2 ligands possibly involved in M···P–M···P–M···triple-bridging bonding between $[Pd_2(PPh_2)H_x]_n$ and $[Pt(PPh_2)]_n$ oligomers in the cluster cores [26]. Strong donor diaryl- and triarylphoshide ligands are known due to their ability to form organometallic complexes with Au, Pd, Pt and Rh and commonly used as auxiliary ligands in catalytic systems for hydrogenation [2,26,34]. So, because of strong metal–ligand interactions, the three-layer Au_{55} core in the $Au_{55}[PPh_3]_{12}Cl_6$ cluster behaves as a non-metallic if it has an intact ligand shell, but the transition to metallic state occurs after partial decomposition of the ligand shell initiated by the removal of the Cl atoms [35]. At the higher metal-to ligand ratio, clusters (**III**) with larger five-shell Pd cores stabilized by weaker 1,10-phenanthroline or 2,2′-bipyridine ligands in the inner coordination sphere and acetate anions in the outer coordination sphere [33] display essentially colloidal metal polyhedral crystalline structures similarly to 1–2 nm diameter thermally deposited naked Pt particles.

Although data on the catalytic activity of the clusters (**I**) and (**II**) are not available at present time, one can make some suggestions concerning possible relations between their structures and catalytic properties. An aperiodic arrangement of the Pt and Pd cores stabilized with phosphine ligands indicates a non-crystalline state of the metal atoms forming molecular clusters. Ligand stabilized metal nanoclusters in this size range exhibit well pronounced quantum size behavior. The catalytic activity of the clusters also depends on the kind of ligand molecules. All these factors should influence catalytic properties of the clusters (**I**) and (**II**). Similarly to Pd and Pt phosphine complexes [26], cleavage of the C–Ph bond under mild conditions

may be a common catalyzed process for reactions of both Pd and Pt clusters. Giant palladium clusters (**III**) catalyze various oxidative reactions under mild conditions (20–90 °C, 1 atm), such as oxidative acetoxylation of ethylene into vinyl acetate, propylene into ally1 acetate and toluene into benzyl acetate; oxidation of primary aliphatic alcohols into esters, and conversion of aldehydes into acetals [1,7–10]. Unlike palladium, data on platinum giant clusters are still scarce and contradictory. However, it was shown that the Pt clusters stabilized with 1,10-phenanthroline and triphenylphosphine are active in photocatalytic generation of hydrogen from water and hydrogenation of olefins in ethanol at 30 °C under 1 atm hydrogen [6,36]. Due to the more favorable coordination of diphenylphosphine than 1,10-phenanthroline, the activity of clusters (**I**) and (**II**) in both reactions could be lower as compared to (**III**). One could expect in this case higher selectivities because the coordination of diphenylphosphine may block efficiently most parts of the active sites on the surface of the cluster particles while 1,10-phenanthroline may block only edge-like parts of the metal cores.

5. Conclusions

Pd and Pt giant clusters (**I**)–(**III**) of varying ligands and metal-to-ligand ratios were investigated by HRTEM and SAED complemented with integrated high spatial resolution FE-AEM utilizing HAADF-STEM imaging and windowless EDXS and EELS. HRTEM and HAADF-STEM revealed aperiodic Pd and Pt core structures of the clusters (**I**) and (**II**) with average sizes of 1.6 ± 0.3 nm and 1.5 ± 0.3 nm, respectively. Diffuse scattering dominating their SAED patterns was likely caused by a non-periodic perturbation of the metal lattice induced by surface reconstruction/relaxation due to the interaction with strong PPh_2 ligands. This suggests that clusters (**I**) and (**II**) may have no exact chemical composition neither precise ordered structure, but rather composed of statistically distributed units with more or less narrow size and structure distributions similar to colloidal metals. The metal formal oxidation state in such species described by idealized models can be non-integer as for the majority of individual metal clusters. For clusters (**I**), chemical compositions along the line profile converted from the net EEL spectral intensities into atomic ratios with 10% accuracy appeared to be in a fair agreement with the ideal stoichiometry and estimations derived from EDXS data by the Cliff–Lorimer thin film ratio method. Compositional variations along the line profile at some positions, however, exceeded $\pm 10\%$ limits, thus indicating local deviations from the ideal stoichiometry likely starting at the interfaces between Pd cores and ligand shells. Aperiodic Pd and Pt core structures may arise due to a transformation to a non-metallic molecular state induced by the strong binding ligands at relatively low metal-to-ligand ratios possibly involved in M···P–M···P-M···triple-bridging bonding between constituting oligomers in the cluster cores. At the higher metal-to-ligand ratio, clusters (**III**) with larger five-shell Pd cores stabilized by 1,10-phenanthroline ligands in the inner coordination sphere and acetate anions in the outer coordination sphere display essentially colloidal metal polyhedral crystalline structures with an expanded fcc lattice similarly to 1–2 nm diameter thermally deposited reference Pt particles.

Acknowledgements

Author is thankful to Dr. Peter A. Crozier from the Center for Solid State Science, Arizona State University, Tempe, AZ, USA for help in measurements and to Prof. M.N. Vargaftik and Dr. N.Yu. Kozitsyna from N.S. Kurnakov Institute of General and Inorganic Chemistry, Russian Academy of Sciences, Moscow, Russian Federation for providing the Pt and Pd cluster samples and valuable discussions. The research was partly supported by the US Department of Energy, under contract DE-FG02-01ER45918.

References

[1] I.I. Moiseev, M.N. Vargaftik, in: J.A. Tomas, K.I. Zamaraev (Eds.), Perspectives in Catalysis, Blackwell, London, 1992, p. 91.
[2] J.D. Aiken, R.G. Finke, J. Mol. Catal. A Chem. 145 (1999) 1.
[3] H. Bonnneman, R.M. Richards, Eur. J. Inorg. Chem. (2001) 2455.
[4] I. Efremenko, J. Mol. Catal. A 173 (2001) 19.
[5] P. Chini, Gas. Chim. Ital. 109 (1979) 225.
[6] V.V. Blagutina, A.I. Kokorin, V.P. Oleshko, V.Y. Shafirovich, Docl. Akad. Nauk. SSSR 314 (1990) 882.
[7] I.I. Moiseev, M.N. Vargaftik, T.V. Chernysheva, T.A. Stromnova, A.E. Gekhman, G.A. Tsirkov, A.E. Makhlina, J. Mol. Catal. A Chem. 108 (1996) 77.
[8] M.K. Starchevsky, S.L. Hladyi, Y.A. Pazdersky, M.N. Vargaftik, I.I. Moiseev, J. Mol. Catal. A Chem. 146 (1999) 229.
[9] I.I. Moiseev, T.A. Stromnova, M.N. Vargaftik, S.T. Orlova, T.V. Chernysheva, I.P. Stolarov, Catal. Today 51 (1999) 595.
[10] S.S. Hladyi, M.K. Starchevsky, Y.A. Pazdersky, M.N. Vargaftik, I.I. Moiseev, Mendeleev Commun. 2 (2002) 1.
[11] G. Kovtun, T. Kameneva, S. Hladyi, M. Starchevsky, Y. Pazdersky, I. Stolaroov, M. Vargaftik, I. Moiseev, Adv. Synth. Catal. 344 (2002) 957.
[12] Y. Volokitin, J. Sinzig, L.J. de Jong, G. Schmid, M.N. Vargaftik, I.I. Moiseev, Nature 384 (1996) 621.
[13] P.M. Paulus, A. Goessens, R.C. Thiel, A.M. van der Kraan, G. Schmid, L.J. de Jongh, Phys. Rev. B 64 (2001), 205418–1.
[14] G. Schmid, J. Chem. Soc. Dalton Trans. 7 (1998) 1077.
[15] G. Schmid, N. Beyer, Eur. J. Inorg. Chem. 5 (2000) 835.
[16] S. Liu, R. Maoz, G. Schmid, J. Sagiv, Nanoletters 2 (2002) 1055.
[17] D. Wyrwa, N. Beyer, G. Schmid, Nanoletters 2 (2002) 419.
[18] T. Reuter, O. Vidoni, G. Schmid, Nanoletters 2 (2002) 709.
[19] O. Vidoni, S. Neumeier, N. Bardou, J.-L. Pelouard, G. Schmid, J. Cluster Sci. 14 (2003) 325.
[20] G. Schmid, J. Mater. Chem. 12 (2002) 1231.
[21] Z.L. Wang, in: Z.L. Wang (Ed.), Characterization of Nanophase Materials, Wiley-VCH, Weinheim, 2000, p. 37.
[22] P. Batson, Ultramicroscopy 96 (2003) 239.
[23] A.I. Kirkland, J.M. Titchmarsh, J.L. Hutchinson, D.J.H. Cockayne, C.J.D. Hetherington, R.C. Doole, H. Sawada, M. Haider, P. Hartell, JEOL News 39 (2004) 2.
[24] G. Schmid, in: M.J. Clarke, et al. (Eds.), Clusters, Structure and Bonding, vol. 62, Springer-Verlag, Berlin, 1985, p. 51.
[25] I.I. Moiseev, R.I. Rudy, N.V. Cherkashina, L.K. Shubochkin, D.I. Kocubei, B.N. Novgorodov, G.A. Kryukova, V.N. Kolomiychuk, M.N. Vargaftik, Inorg. Chim. Acta 280 (1998) 339.
[26] I.I. Moiseev, N.Y. Kozitsyna, D.I. Kochubey, V.N. Kolomijchuk, K.I. Zamaraev, J. Organometal. Chem. 451 (1993) 231.
[27] G. Cliff, G.W. Lorimer, J. Microsc. 103 (1975) 203.
[28] D.B. Williams, B.C. Carter, Transmission Electron Microscopy: A Textbook for Materials Science, Plenum Press, New York, 1996, pp. 351 and 609.

[29] V. Oleshko, R. Gijbels, S. Amelinckx, in: R.A. Meyers (Ed.), Encyclopedia of Analytical Chemistry, Wiley & Sons, Chichester, 2000, p. 9088.
[30] R.F. Egerton, Electron Energy-Loss Spectroscopy in the Electron Microscope, second ed., Plenum Press, New York, 1996, p. 279.
[31] J.W. Niemantsverdriet, in: R.A. van Santen, P.W.N.M. van Leeuwen, J.A. Moulijn, B.A. Averill (Eds.), Catalysis: An Integrated Approach, second ed., Elsevier, Amsterdam, 1999, p. 489.
[32] S.-C.Y. Tsen, P.A. Crozier, J. Liu, Ultramicroscopy 98 (2003) 63.
[33] V. Oleshko, V. Volkov, R. Gijbels, W. Jacob, M. Vargaftik, I. Moiseev, G. Van Tendeloo, Z. Phys. D 34 (1995) 283.
[34] G. Schmid, B. Corain, Eur. J. Inorg. Chem. (2003) 3081.
[35] H.-G. Boyen, G. Kastle, F. Weigl, P. Ziemann, G. Schmid, M.G. Garnier, P. Oelhafen, Phys. Rev. Lett. 87 (2001) 276401.
[36] N. Toshima, K. Nakata, H. Kitoh, Inorg. Chim. Acta 265 (1997) 149.